Isothermal Characterization of Traps in GaN HEMTs Operating in Class B Using a Real-Time Pulsed-RF NVNA Testbed

Miles Lindquist, *Graduate Student Member, IEEE*, Patrick Roblin, *Senior Member, IEEE*,
Dominic Mikrut, *Graduate Student Member, IEEE*, Matthew J. Nichols, *Graduate Student Member, IEEE*,
and Nicholas C. Miller, *Senior Member, IEEE*

Abstract— This article presents a real-time nonlinear vector network analyzer (NVNA) testbed that enables the acquisition of the isothermal transient response of GaN HEMTs operating in pulsed class-B mode with arbitrary loads. An oscilloscope-based architecture and a cost-effective and traceable harmonic phase calibration procedure are presented for the proposed real-time NVNA. The system is configured to realize pulsed multiharmonic active load—pull (ALP) for synthesizing any class of operation. This real-time NVNA is used for the characterization of trapping in GaN HEMTs operating in pulsed class B under verified isothermal operation. It allows for the isothermal acquisition of the RF dynamic loadlines from pulse-to-pulse at different biasing conditions to account for different trapping states and operating temperatures. The capture and emission processes are monitored at each pulse using the quiescent current and RF power for each of the biasing conditions considered. These measurements and associated trap modeling demonstrate that a majority of the capture process is taking place in the first RF pulse (<200 ns) with the residual capture process distributed over various durations depending on the biasing condition and associated temperature. The proposed real-time NVNA combined with pulsed multiharmonic ALP should prove to be a useful tool for studying trapping effects in RF devices.

Index Terms— GaN HEMT, nonlinear vector network analyzer (NVNA), oscilloscope, pulsed-active load—pull (ALP), traps.

I. INTRODUCTION

NONLINEAR vector network analyzers (NVNAs) are instruments used for the large-signal characterization of nonlinear electronic devices at radio frequency (RF) operation. By measuring transistors in the nonlinear regime where they are to be used in practice, as opposed to performing the small-signal measurements with on standard VNAs, one gains a more complete understanding of the device's operation which can be applied when designing devices, modeling devices, or designing RF circuits such as power amplifiers (PAs). Conventional NVNAs are typically suited for characterizing devices operating in a steady state, whether continuous wave (CW) or pulsed, but offer little information about transient effects taking place in the device under test (DUT) before the device reaches a steady state. Thus, there exists a need for a real-time NVNA capable of characterizing the time evolution of the device behavior before a steady state is reached [1].

Let us first consider the suitability of the various NVNA architectures for developing such a real-time NVNA. The first fully-calibrated NVNA reported was the large-signal network analyzer (LSNA) which relies on a subsampling architecture for its measurement of multiharmonic signals [2]. A mixer-based architecture was subsequently reported in [3]. A sampler-based NVNA using a sampling oscilloscope was reported in [4]. Low-frequency, oscilloscope-based analyzers have also recently been developed to reveal CW large-signal loadlines of devices [5], [6]. However, these systems operate at very low frequencies and do not necessarily require rigorous NVNA calibration.

These standard NVNAs can acquire CW, pulsed, or modulated waveforms, but there are limitations based on the architecture of the instrument. In particular, NVNAs using mixer-based and subsampling architectures require steady-state, periodic CW, or modulated signals. Mixer-based NVNAs measure each harmonic frequency (and modulation tones) at different times, thus requiring the signals to repeat over multiple periods and pulses in order to complete a full measurement of the signal. Subsampling NVNAs use a comb generator with a low sampling frequency to sample the periodic modulated multiharmonic RF signals, and therefore also require an acquisition over multiple modulation periods and pulses.

Clearly, the mixer-based and subsampling-based NVNAs rely on equivalent time and cannot be used for the acquisition of pulsed-RF signals which can slowly vary from pulse to pulse. These instruments used for large-signal measurement of RF devices test them in a steady-state condition, aggregating and averaging the measured results across a multitude of periods and pulses. A real-time sampler-based NVNA architecture

able to acquire each pulse in its entirety is required for such types of signals.

The device's behavior preceding the steady-state operation offers useful information about the memory effects affecting it. A particularly salient example of these transient effects is traps in GaN HEMTs that fill with electrons when high drain voltages are applied [7], [8], [9], [10], [11], [12], [13]. The current collapse that results from the high drain voltage is ascribed to trapping from dopants and defects in the GaN buffer layer beneath the 2DEG channel [9]. The traps are most certainly filled by the dc bias of the transistor, but will also further fill under large-signal RF operation. As the transistor operates along its loadline and swings at high frequency to instantaneous drain voltages larger than the bias voltage, it will cumulatively fill traps, further degrading the performance of the device past the initial trapping and/or self-heating from its dc bias conditions [15], [16]. This effect, first reported in [17] for C-MOSFETs, is referred to as the cyclostationary effect. The use of pulsed-dc and pulsed-RF excitations is also desirable for isothermal characterization in order to differentiate between self-heating and trapping [15]. A *real-time NVNA* capable of capturing the RF and baseband response of a transistor within a single pulse is thus required to better characterize the trap dynamics from pulse to pulse for arbitrary loadlines. In this study, the focus is placed on class-B operation since this is a common mode of operation in power-efficient amplifiers such as Doherty PAs. A low frequency of operation (50 MHz) will be used to minimize the internal displacement current and monitor the evolution of the class-B loadline.

This article provides detailed information on the construction, calibration, and application of an improved version of the real-time NVNA previously reported by Lindquist et al. [1]. A modified setup for the real-time NVNA is presented in Section II. A more cost-effective and traceable calibration is introduced in Section III. The application of this improved real-time NVNA to pulsed active-load—pull measurements of a GaN HEMT operating in class B for characterizing traps at a variety of bias conditions is then presented in Section IV. An isotrap RF loadline is introduced to verify that the operation is isothermal even up to 400 pulses. A behavior model is used to identify the leading time constants involved in the trap emission and capture processes under isothermal RF operation. A summary of the achievements is then presented in Section V.

II. ARCHITECTURE OF THE REAL-TIME NVNA

The real-time NVNA reported in [1] relies on two separate oscilloscopes. The RF oscilloscope (Tektronix MSO64B) is connected to two dual-directional couplers to measure the large-signal incident and reflected RF waveforms at each port. The baseband oscilloscope (Tektronix DPO7254) is used to acquire the dc and/or pulsed biases via oscilloscope-specific voltage and current probes.

The time-base of both oscilloscopes is phase-locked. The oscilloscopes used in this NVNA have a segmented memory function which provides the capability of repeatedly recording specified lengths of data when externally triggered to avoid

recording between the RF and bias pulses. This greatly reduces data storage and accelerates data transfer when a multitude of pulses (400 in this work) are applied.

The original setup reported at [1] has been modified by removing the highpass filters in the RF path and adding an optional transformer ac current probe between the bias tee and the device. The transformer ac current probe supplements the Hall effect current probe (Tektronix TCP0030), which would introduce too much inductance to place in the RF path between the bias tee and transistor. High-impedance voltage probes (Tektronix P6139A) are used on the baseband path preceding both RF bias tees to measure the transient gate and drain voltage. A higher bandwidth oscilloscope and wider bandwidth couplers (Werlatone C7646DC) are now used in the testbed. The modified setup can be seen in Fig. 1.

Each port of the NVNA is connected to its own pair of bias tees consisting of the baseband bias tee (AvTech AVX-TD) which combines the pulses and dc, and the RF bias tee (INMET 8860SFM2-02) that combines the baseband and RF signals. The frequency span for the dc path of the RF bias tee model is dc to 30 MHz.

The low-pass filters (Mini-Circuits SLP-36+) seen in Fig. 1 are used to filter out any higher frequency components of the pulse that may leak through to the ac path of the RF bias tees, as well as prevent the pulse's higher frequencies components from leaking through back to the RF path. These are considered optional depending on the RF frequency and pulsewidth used for the measurement and are marked as such in Fig. 1. The sources used for the pulsed-RF and pulsed-bias excitations are arbitrary wave generators (AWGs) capable of generating triggered bursts, enabling precise control over the excitation duration and the sequencing of each measurement. One port of the AWG (Teledyne T3AFG350) was used to pulse the gate of the transistor, while the other port triggered the high-voltage pulse generator (AvTech AV-1011-C-OP1B) connected to the drain side of the testbed. Employing AWGs as the real-time NVNA's sources allows for a variety of pulsed multiharmonic active load—pull (ALP) measurements to be made with minimal reconfiguration of instrumentation. In particular, no multiplexer is needed to combine harmonics with this approach.

An alternative setup was also investigated in which the couplers are placed between the bias tees and the ports of the DUT. One disadvantage of this approach is that the couplers were found to increase the ringing duration of the pulsed bias signals applied to the devices.

The instrumentation described above excels at capturing low-frequency, pulsed-RF measurements to characterize a device's loadline in transient states before settling into steady-state operation. There are, however, some limitations when using an oscilloscope-based architecture. Since the bandwidth of real-time oscilloscopes are limited by the sampling rate in comparison to mixer-based and subsampling NVNA architectures, the maximum frequency of the oscilloscopes will limit the frequency at which multiharmonic measurements can be performed. In addition, on account of an oscilloscope's time-domain data capture, each receiver can measure the instrument's full frequency band, introducing more noise to the
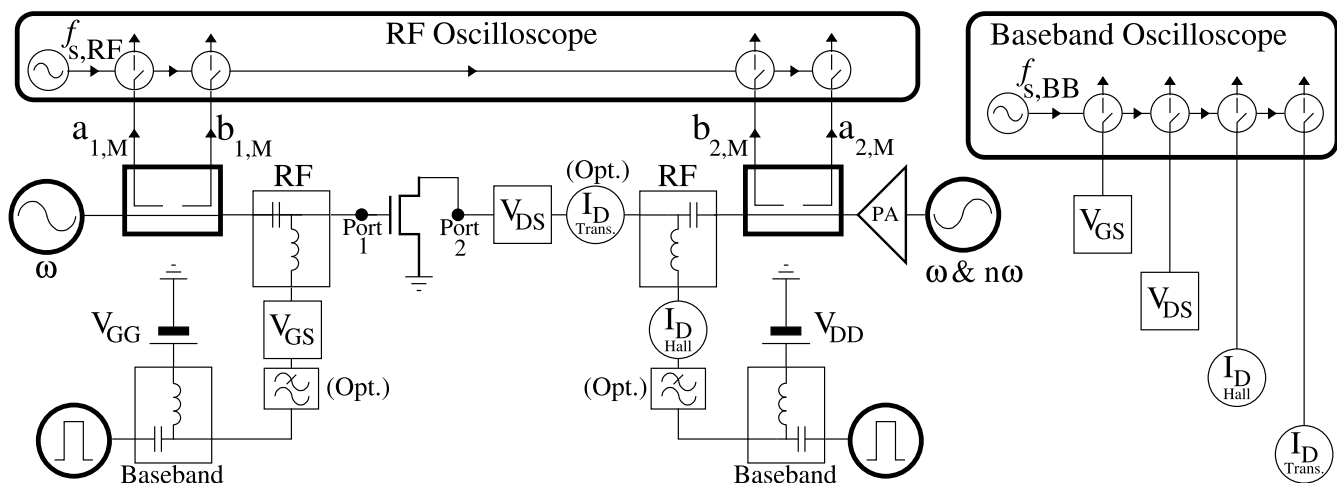
This article has been accepted for inclusion in a future issue of this journal. Content is final as presented, with the exception of pagination.

LINDQUIST et al.: ISOTHERMAL CHARACTERIZATION OF TRAPS IN GaN HEMTs OPERATING IN CLASS B   3

Fig. 1.   Diagram of the equipment utilized for pulsed large-signal RF measurement of transistors. All oscilloscopes and signal generators are programed via PC and triggered from a delay generator.

measurement than other NVNA architectures. Oscilloscopes will typically allow the user to limit the bandwidth on each channel, which can mitigate this issue.

III. Modified NVNA Calibration

Like all NVNAs, it is necessary to calibrate this oscilloscope-based NVNA at the DUT's reference ports using NVNA calibration techniques, to account for the dispersion (loss and phase shift) introduced by the testbed in the signal path. A calibration method for this testbed that used measurements from a calibrated mixer-based NVNA was previously reported by Lindquist et al. [1]. A correction of an error in one of the equations in that publication is reported in Appendix A. In this article, an alternative calibration scheme is developed.

Typical NVNA calibration protocol involves three separate measurements, vector calibration using known standards: short, open, load, and thru (SOLT), power calibration, and harmonic phase reference (HPR) calibration. The power calibration measures the amplitude of the wave at the device's reference planes and compares it to the amplitude of the wave measured by the oscilloscope at each frequency considered. The HPR calibration measures a harmonic-rich signal at the fundamental frequency to determine the effect of all of the components present in the RF path on the signal's phase at each harmonic relative to the fundamental frequency. These measurements must be repeated for all the harmonics acquired [18]. The three calibration steps mentioned above provide measured data for the calibration matrix $\mathbf{T}_i(n\omega)$, which is shown factored as $A_i(n\omega)\overline{\mathbf{T}}_i(n\omega)$ in the following equation:

$$
\begin{bmatrix} a_{i,M}(n\omega) \\ b_{i,M}(n\omega) \end{bmatrix} = A_i(n\omega) \begin{bmatrix} 1 & B_i'(n\omega) \\ C_i'(n\omega) & D_i'(n\omega) \end{bmatrix} \begin{bmatrix} a_i(n\omega) \\ b_i(n\omega) \end{bmatrix}
$$
$$
= A_i(n\omega) \cdot \overline{\mathbf{T}}_i(n\omega) \begin{bmatrix} a_i(n\omega) \\ b_i(n\omega) \end{bmatrix} \quad (1)
$$

where $a_{i,M}$ and $b_{i,M}$ are the oscilloscope measurements at the coupled ports, while a_i and b_i are the incident and reflected waves at port i of the DUT. The vector calibration using

standard short, open, and load terminations on an impedance standard substrate (ISS) is performed with on-wafer probes (FormFactor ACP40-GSG-125) at each frequency $n\omega$ for each port i to determine B_i', C_i', and D_i'. Since both the power and HPR calibrations are performed at the coaxial port connected to the probes, the loss and dispersion introduced by the on-wafer probes have been characterized through a separate SOL measurement on an ISS using a VNA. The results are shown in Table I. The data provides a very small amplitude and phase correction to be introduced in the power and HPR calibration, respectively.

A. Amplitude Calibration With Power Meter

A power meter is connected to port 1 to determine the loss through the signal path to be calibrated. The power of the signal at port 1 is compared with the measured signals at the corresponding oscilloscope ports to account for the loss associated with the cabling, coupler, and other components in the signal path. This relation is recorded as $|A_1|$ in the following equation:

$$
|A_1(n\omega)| = \frac{|a_{1,M}(n\omega)|/\sqrt{Z_0}}{|1 + B_1'(n\omega)\Gamma_P(n\omega)|} \sqrt{\frac{1 - |\Gamma_P(n\omega)|^2}{2P(n\omega)}} \quad (2)
$$

where

$$
\Gamma_P(n\omega) = \frac{b_{1,M}(n\omega) - C_1'(n\omega)a_{1,M}(n\omega)}{D_1'(n\omega)a_{1,M}(n\omega) - B_1'(n\omega)b_{1,M}(n\omega)}.
$$

For this setup, $Z_0 = 50$ Ω and $P(n\omega)$ refers to the power in Watts measured by the power meter. Modern power meters have NIST-traceable calibrations, so there is no extra validation required for this step.

B. HPR Calibration Using an AWG

Standard HPR calibration of mixer-based NVNAs requires the use of two comb generators. The output of one of these comb generators is sent directly to one of the NVNA's receivers to establish a phase reference, given that the measurement of the different harmonics is performed at different
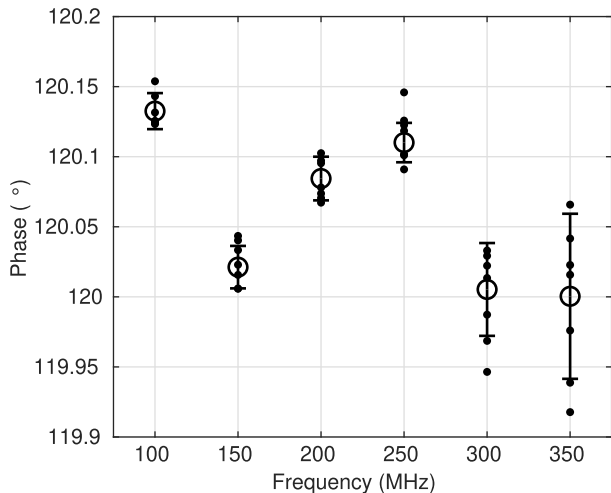
Fig. 2. Measured phase of calibrated $b_1(n\omega)$ with an alternative programed phase used to check the accuracy and precision of the HPR calibration. The programed phase for each harmonic was set to 120° relative to the fundamental frequency of 50 MHz for this verification, instead of the programed 72° for the calibration.

TABLE I
DISPERSION AND INSERTION LOSS OF WAFER PROBES

Freq. (MHz)	Probe Dispersion (°)	Std. Dev Probe (°) Dispersion	Probe Loss (dB)	Std. Dev. Probe Loss (dB)
50	0	0	0.0368	0.0027
100	0.05	0.05	0.0228	0.0033
150	0.09	0.07	0.0403	0.0035
200	0.15	0.12	0.0380	0.0093
250	0.19	0.12	0.0427	0.0074
300	0.24	0.15	0.0479	0.0099
350	0.28	0.15	0.0509	0.0089

times. The second comb generator's output is sent to port 1 to characterize the changes in the harmonics phase relative to the fundamental as the signal travels through the entire RF signal path.

Comb generators can be used as an effective phase reference to calibrate mixer-based NVNAs. However, the use of comb generators to calibrate oscilloscope-based NVNAs is not desirable because they generate pulses with a high peak-to-average power ratio and thus require receivers with a high dynamic range (HDR).

This article will detail an alternative approach to achieve the same HPR characterization of the dispersion of the real-time NVNA's signal path when using a receiver with a lower dynamic range. Instead of employing a comb generator to generate a harmonic-rich signal, an AWG can be programed to create a dual-tone signal that combines the fundamental frequency with a harmonic with a set phase difference. The programed phase difference between the fundamental and harmonic will persist in the transmission line until it reaches a dispersive component. Once the oscilloscope's receivers measure the phase-shifted signal, the difference $\phi(n\omega) - n\phi(\omega)$ for the nth harmonic between the two frequencies phases can be measured to determine the necessary compensation that must be performed to accurately characterize the signal at the port being calibrated.

The combined fundamental and harmonic signal is sent from port 1 backward through the dispersive signal path of the testbed seen in Fig. 1 (bias tees and coupler). The power level is on the order of a few dBm.

When performing the described HPR calibration, it is recommended to terminate the other end of the signal path (normally the input) with a matched load. The measured signal, $b_{1,M}$, is measured by the oscilloscope, and then converted to the frequency domain. Once in frequency domain the phase of $b_{1,M}(n\omega)$ is reset to

$$\angle[b_{1,M}^{\text{reset}}(n\omega)] = \angle[b_{1,M}(n\omega)] - n\angle[b_{1,M}(\omega)] \quad (3)$$

so that $\angle[b_{1,M}^{\text{reset}}(\omega)] = 0$. Then, from the relation between the incident and reflected waves at port 1 and the measured waves

$$\begin{bmatrix} a'_{1,\text{HPR}}(n\omega) \\ b'_{1,\text{HPR}}(n\omega) \end{bmatrix} = A_1(n\omega) \begin{bmatrix} a_{1,\text{HPR}}(n\omega) \\ b_{1,\text{HPR}}(n\omega) \end{bmatrix}$$
$$= \overline{\mathbf{T}}_1^{-1}(n\omega) \begin{bmatrix} a_{1,M}^{\text{reset}}(n\omega) \\ b_{1,M}^{\text{reset}}(n\omega) \end{bmatrix} \quad (4)$$

where

$$n = 1, 2, 3, \ldots$$

we can solve for the angle $\theta(n\omega)$ of $A_1(n\omega) = |A_1(n\omega)|e^{j\theta(n\omega)}$

$$\theta(n\omega) = \angle[b'_{1,\text{HPR}}(n\omega)] - n\angle[b'_{1,\text{HPR}}(\omega)] - \Psi_{\text{prog}}(n\omega) \quad (5)$$

where $\Psi_{\text{prog}}(n\omega)$ is the programed HPR phase in the AWG.

To determine the accuracy and precision of the HPR calibration with the AWG, seven verification measurements where the phase of the harmonics is set to a different angle than $\Psi(n\omega)$, the programed angle used for the calibration, are also performed when the AWG is connected to port 1.

After performing the inverse of (1) with the results of this validation measurement, the alternative programed angle should be retrievable from $\angle[b_1(n\omega)]$. An example of this is plotted in Fig. 2 with the nominal programed angle set to 120° relative to the fundamental frequency's phase for all harmonics. The mean phase deviated by 0.3° from the target phase while the maximum deviation from each mean was approximately 0.1°.

C. Thru Calibration

Once the values of $A_1(n\omega)$ have been determined, the coefficients $A_2(n\omega)$ are obtained using the ratios $A_2(n\omega)/A_1(n\omega)$ obtained from the thru calibration of the following equation:

$$\begin{bmatrix} a_{1,M}(n\omega) \\ b_{1,M}(n\omega) \end{bmatrix} = \frac{A_1(n\omega)}{A_2(n\omega)} \overline{\mathbf{T}}_T(n\omega) \begin{bmatrix} a_{2,M}(n\omega) \\ b_{2,M}(n\omega) \end{bmatrix} \quad (6)$$

where

$$\overline{\mathbf{T}}_T(n\omega) = \overline{\mathbf{T}}_1(n\omega)\mathbf{T}_{\text{thru}}\overline{\mathbf{T}}_2^{-1}(n\omega).$$

The values of $A_1(n\omega)$ and $A_2(n\omega)$ are then multiplied by $\overline{\mathbf{T}}_1$ and $\overline{\mathbf{T}}_2$, respectively, to yield the denormalized matrices: $\mathbf{T}_1(n\omega) = A_1(n\omega)\overline{\mathbf{T}}_1(n\omega)$ and $\mathbf{T}_2(n\omega) = A_2(n\omega)\overline{\mathbf{T}}_2(n\omega)$.

This article has been accepted for inclusion in a future issue of this journal. Content is final as presented, with the exception of pagination.

LINDQUIST et al.: ISOTHERMAL CHARACTERIZATION OF TRAPS IN GaN HEMTs OPERATING IN CLASS B   5
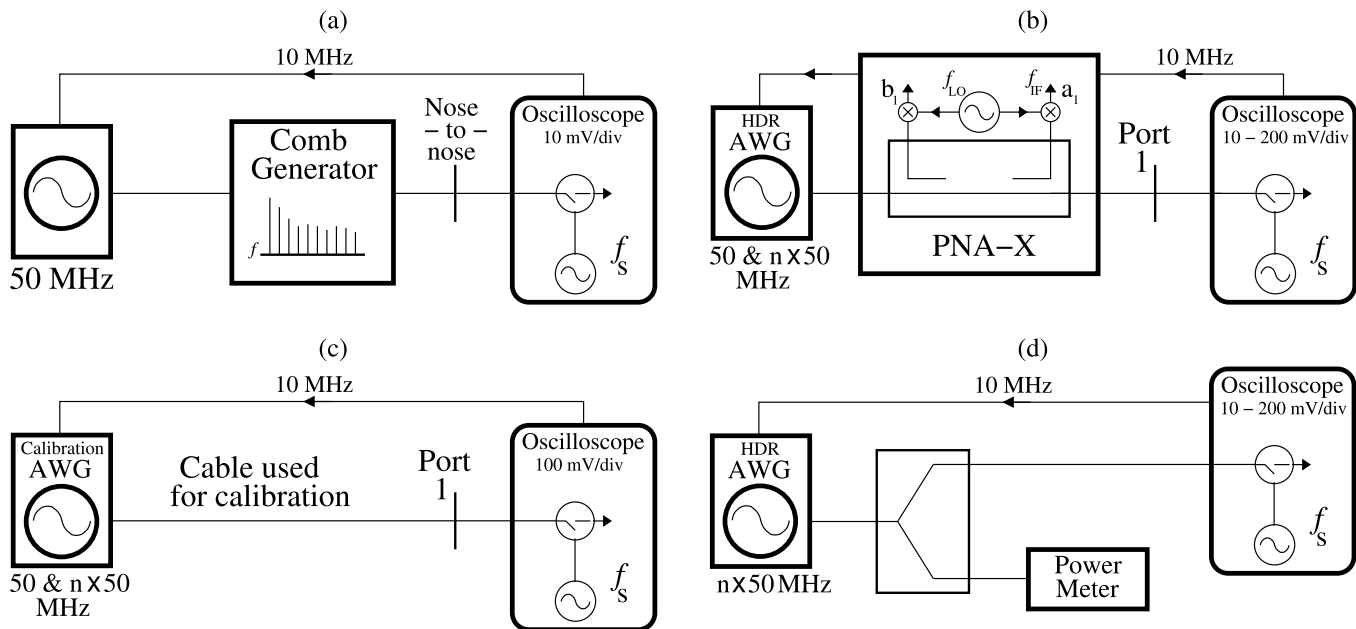

Fig. 3. Various measurement setups used for characterization of nonlinear effects from instruments. (a) NIST-traceable comb generator's output is measured as a standard to quantify the nonlinearity of the oscilloscope's internal components. (b) Dual-tone measurements from an AWG with HDR are measured by a PNA-X in NVNA mode in cascade with the oscilloscope to determine if any dispersion is introduced by changing the oscilloscope's voltage scaling. (c) Output from the calibration AWG and cable is directly measured by the oscilloscope to account for dispersion from the AWG. (d) Measured amplitude of a signal at various powers and associated oscilloscope voltage scalings is compared against the measurement of a power meter.

D. Standard Transfer, Scaling Characterization, and Correction

Though the previously detailed HPR calibration procedure has been shown to be self-consistent, its dependence on the AWG calibration accuracy and the vertical scaling of the oscilloscope needs to be investigated.

In this work, the real-time NVNA (scope and testbed) is calibrated using a reference AWG with a maximum frequency of 6 GHz (Tektronix AWG7122B). There is a possibility that the internals of the AWG and the cable used to connect it to port 1 could introduce dispersion. In the context of the calibration, dispersion introduced here would mean that the programed harmonic phase $\Psi(n\omega)$ is not the exact phrase received at port 1, and therefore must be compensated for when programming waveforms are used for calibration.

In Sections III-D1–III-D4, the accuracy of the AWG used in the calibration will be evaluated using a 50 GS/s oscilloscope whose accuracy itself has been verified using a NIST-traceable comb generator.

Four separate measurements were conducted to determine the level of nonlinearity in amplitude and phase inherent in the instruments used for the testbed calibration. For clarity in these sections, programed or reference phases are denoted with Ψ, and measured phases are denoted with ϕ.

1) Direct Oscilloscope Measurement of Comb Generator: Before characterizing the AWG, the accuracy of the oscilloscope for HPR measurement below 350 MHz (seven harmonics) must be verified. To confidently determine the level of dispersion introduced by the oscilloscope's internal components, a comb generator (Keysight U9391C) capable of producing harmonics up to 26.5 GHz is measured *nose-to-nose* with the oscilloscope as shown in Fig. 3(a). The comb generators have a NIST-traceable calibration and include

TABLE II
COMPARISON OF COMB GENERATOR CALIBRATION AND MEASURED DATA

Freq. (MHz)	$\Psi_{\text{comb}}^{\text{table}}$ (°)	ϕ_{scope}^{10} (°)	$\Delta\phi_{\text{scope}}^{10,\text{comb}}$ (°)	Std. Dev. ϕ_{scope}^{10} (°)
50	0	0	0	0
100	-179.74	-179.67	0.07	0.10
150	0.53	0.28	-0.25	0.14
200	-179.16	-179.59	-0.44	0.18
250	1.20	0.51	-0.69	0.22
300	-178.40	-179.39	-0.99	0.27
350	1.98	0.59	-1.39	0.32

generator-specific calibration data that can be accessed by the user. These calibration data, reset with respect to the 50 MHz fundamental tone using (3), are listed in column 2 of Table II. A 50 MHz sine wave was injected at the input of the comb generator and its output was measured at 10 mV/div scaling on the oscilloscope at a sampling rate of 50 GS/s. One hundred separate measurements of a window size of 20 μs with a total of 1000 peaks were measured and averaged to fill columns 3–5 in Table II. The scope measurement error $\Delta\phi_{\text{scope}}^{10,\text{comb}}(n\omega) = \phi_{\text{scope}}^{10} - \Psi_{\text{comb}}^{\text{table}}$ is reported in column 4 of Table II. The maximum difference between the manufacturer-specified phase and measured comb phase is 1.39° at the seventh harmonic (350 MHz) for 10 mV/div.

2) Characterization of Oscilloscope Scaling on Dispersion: Due to the limited dynamic range of oscilloscopes, various vertical scaling settings (voltage ranges) are used for different measurements in this article. The oscilloscope uses voltage scaling units of mV/division (div) for each of its scale settings, with ten divisions comprising its full vertical range. The 10 mV/div scaling is the setting used in every step of the calibration of the real-time NVNA testbed shown in

TABLE III
DIFFERENCE IN MEASURED HARMONIC PHASE BETWEEN OSCILLOSCOPE SCALINGS

Freq. (MHz)	$\Delta\phi_{\text{scale}}^{50,10}$ (°)	$\Delta\phi_{\text{scale}}^{100,10}$ (°)	$\Delta\phi_{\text{scale}}^{200,10}$ (°)
50	0	0	0
100	-0.03	-0.06	-0.24
150	0.53	-0.13	-0.51
200	-0.22	-0.33	-0.68
250	0.02	0.05	-0.67
300	0.05	-0.36	-1.14
350	0.33	-0.52	-0.9

TABLE IV
DEVIATION OF MEASURED PHASE FROM AWG PROGRAMED PHASE

Freq. (MHz)	ϕ_{AWG}^{100} (°)	Std. Dev. ϕ_{AWG}^{100} (°)	$\Delta\Psi_{\text{AWG}}$ (°)
50	0	0	0
100	0.56	0.003	0.52
150	1.00	0.007	1.30
200	1.83	0.007	2.49
250	1.95	0.008	2.62
300	3.04	0.014	4.31
350	4.05	0.012	5.11

Fig. 1. It is also used in the nose-to-nose measurement of the comb generator (see Section III-D1). During the large-signal measurements in this article, the 50 mV/div scaling is used to measure the RF signals incident to and reflected from the transistor's gate. The 100 and 200 mV/div scalings are used to measure the drain's incident and reflected waves, depending on the power output of the transistor. The 100 mV/div scaling is also used when directly measuring the dispersion of the calibration AWG, as discussed in Section III-D3.

The impact of scaling on oscilloscope measurements has been studied in detail in [22] using a calibrated VNA in the framework of *S*-parameter measurements. In this work, we seek instead to quantify the impact of the voltage scaling on a real-time NVNA. In this section, the variation of the harmonic phases relative to the fundamental is characterized as the scaling is changed. Due to the low amplitude of the comb generator's output, it is not possible to use the previous method to check the internal dispersion of the oscilloscope at different scalings without amplifying the signal and thus introducing additional dispersion. Instead, we will opt to perform a measurement of the HDR AWG's (Teledyne T3AFG350) dual-tone output by cascading a PNA-X in NVNA mode and the oscilloscope as shown in Fig. 3(b). The calibrated PNA-X ensures that the same harmonic phase relative to the fundamental phase is applied at the input of the oscilloscope for each power level and associated oscilloscope scaling used. We note that the AWG used for this measurement is a different AWG than is used for the HPR calibration due to the output power limitation of the calibration AWG. The maximum frequency that can be produced by this HDR AWG is 350 MHz. Table III shows the differences between the measured phase of the AWG's signal at various scalings in reference to the 10 mV/div scaling used in the measurement of the comb. The variation in harmonic phase is calculated for a given scaling X in mV/div as: $\Delta\phi_{\text{scale}}^{X,10}(n\omega) = \phi_{\text{scope}}^{X}(n\omega) - \phi_{\text{scope}}^{10}(n\omega)$. Table III shows that the maximum difference in measured harmonic phase is $-1.14°$. These very small dispersion corrections will be applied to each of the measured harmonics of $a_{i,M}(n\omega)$ and $b_{i,M}(n\omega)$ up to 350 MHz for when the scope scaling is changed.

3) Direct Oscilloscope Measurement of Calibration AWG: After characterizing the oscilloscope's internal scaling circuitry, the AWG used for calibration can be directly measured with the oscilloscope to determine the deviation of the harmonic's phase from the programed phase, $\Psi_{\text{AWG}}^{\text{prog}}(n\omega)$. For this measurement, the calibration AWG was connected to

the testbed's oscilloscope with the same cable that connects the AWG to port 1 during the HPR calibration as shown in Fig. 3(c). A series of dual-tone signals where, the fundamental frequency is combined with one of its harmonics, is generated by the AWG and measured by the oscilloscope. This was repeated seven times for all harmonics and the average of the measured dispersion $\Psi_{\text{AWG}}^{100}(n\omega) - n\Psi_{\text{AWG}}^{100}(\omega)$ are reported in the second column of Table IV. The standard deviation for these measurements is shown in the third column of Table IV. A weak trend of growing dispersion is observed as the frequency increases. Since Ψ_{AWG}^{100} was measured at a vertical oscilloscope scaling of 100 mV/div, it is necessary to correct for the small shift in phase ($\Delta\phi_{\text{scale}}^{100,10}$) documented in Table III that arise from changing the oscilloscope's vertical scaling. We can also correct for the slight discrepancy between the comb generator's manufacturer-calibrated phase and the oscilloscope's measurement of the comb generator at 10 mV/div scaling by subtracting $\Delta\phi_{\text{scope}}^{10,\text{comb}}$. These steps are combined in the simple transfer (7) to yield the corrected $\Psi_{\text{AWG}}^{\text{corr}}$ to be used during the HPR calibration

$$\Psi_{\text{AWG}}^{\text{corr}}(n\omega) = \phi_{\text{AWG}}^{100}(n\omega) - \Delta\phi_{\text{scale}}^{100,10}(n\omega) - \Delta\phi_{\text{scope}}^{10,\text{comb}}(n\omega). \tag{7}$$

Seen in the fourth column of Table IV, the dispersion correction value $\Delta\Psi_{\text{AWG}}(n\omega)$ at all harmonics *n* for the calibration AWG, is obtained by subtracting $\Psi_{\text{AWG}}^{\text{corr}}(n\omega)$ from the programed phase $\Psi_{\text{AWG}}^{\text{prog}}(n\omega)$

$$\Delta\Psi_{\text{AWG}}(n\omega) = \Psi_{\text{AWG}}^{\text{prog}}(n\omega) - \Psi_{\text{AWG}}^{\text{corr}}(n\omega).$$

4) Characterization of Oscilloscope Scaling on Measured Magnitude: A separate measurement is performed to quantify the effect of the oscilloscope's scaling circuitry on the amplitude of a measured signal at the frequencies considered. The measurement setup used, shown in Fig. 3(d), consists of a single-tone signal injected into a power splitter connected to the oscilloscope and a power meter used for reference. The amplitude for each test signal is set commensurate to the scaling considered. For each level of oscilloscope scaling, the amplitudes recorded by each instrument are normalized relative to the measurement at the 10 mV/div scaling, $O_{\text{x},10} = O_{\text{x}}/O_{10}$ and $P_{\text{x},10} = P_{\text{x}}/P_{10}$ for the oscilloscope and power meter's measurements, respectively. A second ratio between the two instruments' measurements at each scaling is calculated to quantify the extent of the amplitude error introduced when switching the oscilloscope scaling: $\gamma_{\text{scale}}^{\text{x},10} = O_{\text{x},10}/P_{\text{x},10}$ and is reported in decibels in Table V. The data indicate that

This article has been accepted for inclusion in a future issue of this journal. Content is final as presented, with the exception of pagination.

LINDQUIST et al.: ISOTHERMAL CHARACTERIZATION OF TRAPS IN GaN HEMTs OPERATING IN CLASS B 7

TABLE V
DIFFERENCE IN MEASURED MAGNITUDE
BETWEEN OSCILLOSCOPE SCALINGS

Freq. (MHz)	$\gamma_{\text{scale}}^{50,10}$ (dB)	$\gamma_{\text{scale}}^{100,10}$ (dB)	$\gamma_{\text{scale}}^{200,10}$ (dB)
50	-0.006	-0.089	-0.015
100	-0.042	-0.137	-0.052
150	-0.050	-0.154	-0.089
200	-0.085	-0.211	-0.113
250	-0.111	-0.255	-0.138
300	-0.161	-0.310	-0.192
350	-0.128	-0.270	-0.143

increasing the scaling of the oscilloscope causes a slightly lower amplitude to be measured by the scope, the extent of which increases with the frequency measured. The largest difference measured (-0.31 dB) is at the 100 mV/div scaling.

IV. APPLICATION OF THE REAL-TIME NVNA FOR PULSED-ALP MEASUREMENTS

We shall consider the application of the real-time NVNA for the isothermal characterization of a transistor using pulsed-ALP measurements. The objective is to study isothermal trapping in a transistor in the absence and presence of self-heating, given the impact of device temperature on the knee walkout has already been well-established [15], [19]. For this measurement, the pulsed class-B loadlines allow for a simultaneous stressing and measurement of the device's behavior. Since GaN HEMTs are used to realize high-efficiency PAs, class-B measurements will be used for a more realistic investigation. The NVNA calibration is applied to the measured time-domain data by first converting them to frequency-domain *in each RF period separately for each pulse* and applying the inverse of $\mathbf{T}_i$ from (1) before returning the data to time domain. This approach is only applicable when the memory effects are slowly varying compared to the RF period.

A. Class-B Pulsed-ALP

In this section, a set of class-B pulsed-ALP measurements are performed on a couple of 2×50 μm GaN HEMTs with a 140-nm gate length and SiN passivation from the same wafer to investigate how are traps filled as the RF operation of the device progressively affects its performance. Class-B measurements were first performed via CW multiharmonic ALP from the HDR AWG. A custom algorithm was developed to iteratively determine the multiharmonic injected waves required to maintain class-B operation. A class-B loadline with a fundamental impedance of $R_L = 294$ Ω was synthesized. The second harmonic reflection coefficient of $\Gamma_L(2\omega) = 0.95 \angle 180.3°$ was actively implemented. The third harmonic reflection coefficient was found to be difficult to control but the third harmonic voltage was around 0.1997 V which is relatively small compared to the fundamental of 12.7 V.

The same AWG's multiharmonic gate and drain waveforms found in these CW ALP measurements were employed for the pulsed-ALP measurements reported here.

Seven harmonics are used in the Fourier Series in all the measurements. Five different biasing conditions are applied to
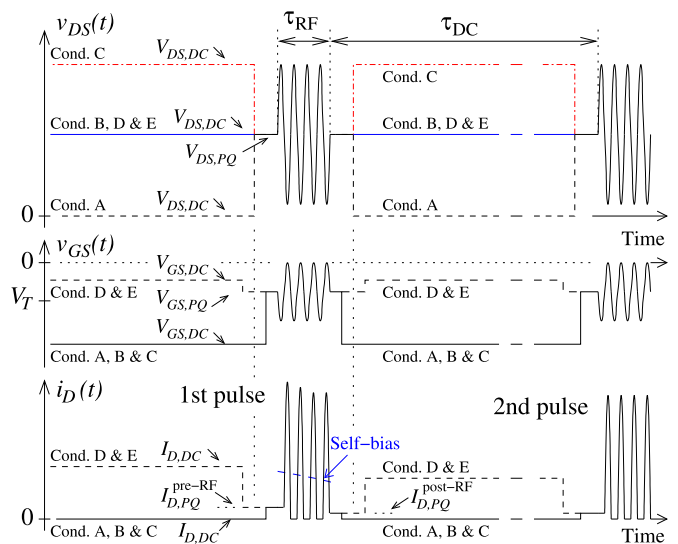

Fig. 4. Diagram showing the sequencing of the gate and drain voltage pulses in relation to the pulsed-ALP for each bias condition.

the device to isothermally test the effects of trapping that result from transistor biasing and the cyclostationary effect from large RF excitations [17]. The five different biasing conditions with and without self-heating are defined as follows.

A) Room temperature with no drain bias: $V_{\text{GS,dc}} = -4.25$ V, $V_{\text{DS,dc}} = 0$ V, $I_{\text{D,dc}} = 0$ mA.
B) Room temperature at V_{DD}: $V_{\text{GS,dc}} = -4.25$ V, $V_{\text{DS,dc}} = 20$ V, $I_{\text{D,dc}} = 0$ mA.
C) Room temperature at $V_{\text{DS,MAX}}$: $V_{\text{GS,dc}} = -4.25$ V, $V_{\text{DS,dc}} = 34$ V, $I_{\text{D,dc}} = 0$ mA.
D) Class-B operating temperature, $P_{\text{dc}} = 0.28$ W: $V_{\text{GS,dc}} = -3.01$ V, $V_{\text{DS,dc}} = 20$ V, $I_{\text{D,dc}} = 14$ mA.
E) High temperature operating condition, $P_{\text{dc}} = 0.56$ W: $V_{\text{GS,dc}} = -2.61$ V, $V_{\text{DS,dc}} = 20$ V, $I_{\text{D,dc}} = 28$ mA.

Conditions A–C highlight the impact of bias on trapping and the associated temporal response. While the device operates at room temperature under conditions A–C, it operates above room temperature in conditions D and E. Conditions D and E show the effect of the transistor temperature on trapping at the same drain voltage as condition B, taken here as the quiescent drain bias V_{DD} for the initial CW loadline.

The intent for measuring the transistor at these distinct biasing conditions was to delineate the relative effects of biasing and self-heating that lead to current collapse in the transistor, and to characterize the time response for the capture and emission processes in the GaN HEMT under both the dc and large-signal RF operating conditions. Class-B operation was chosen because of its relative ease to accomplish via pulsed-ALP, the reduced self-heating introduced from the pulsed-bias conditions, as well as its more common use in modern PAs.

Conditions A–C were biased 1 V below the gate bias voltage used for the CW class-B measurement to explore different trap-filling states with negligible self-heating. For all conditions, the gate and drain voltages were pulsed up or down to the pulsed-quiescent (PQ) class-B operating point:

$V_{GS,PQ} = -3.25$ V and $V_{DS,PQ} = 21.5$ V. The PQ bias point $V_{GS,PQ}$ is the same bias point used to bias the device when synthesizing the CW loadline of the device. The quiescent drain current of the transistor at this bias point was approximately 6 mA. A relatively high quiescent drain bias current was selected so that the *PQ* drain current during the pulsed-ALP measurements would not reduce to zero before the trap capture saturates. The PQ drain bias voltage was pulsed slightly higher than 20 V to compensate for an observed temporary decrease in the measured pulsed drain voltage bias during the transistor's class-B self-biasing. This ensured that the device was approximately reaching the same peak drain voltage that it did during the CW measurement.

For the measurements detailed here, the drain PQ voltage was pulsed for 1.7 μs and the gate PQ voltage was pulsed for 1.2 μs when biased at conditions A–C to protect the device from damaging current/power spikes. For the thermal biasing conditions D and E, the gate PQ voltage was instead pulsed for 1.7 μs and the drain PQ voltage was pulsed for 1.2 μs for the same reason. During each pulse, class-B pulsed ALP at 50 MHz was applied for ten periods of 50 MHz ($\tau_{RF} = 200$ ns). The specific sequencing of the pulsed measurement for each condition is shown in Fig. 4.

B. Large-Signal Measurements

The loadlines used to stress the device can be examined to track the performance of the device as it operates over the course of the measurement. Instead of operating the device in the low-efficiency class-A mode to stress the device, like those seen in Fig. 3(a) in [1], we are using the more power-efficient class-B operating mode so that the cyclostationary effect is now activated by a more conventionally used loadline.

Fig. 5(a)–(e) shows the pulsed-IV curves and loadlines at pulse 1 and pulse 400 biased at conditions A–E. The associated voltage and current waveforms are shown in Fig. 6. The pulsed-ALP experiments with the real-time NVNA were performed for the five conditions described above with a pulse repetition period of 100 μs. The pulsed-IV measurements were carried out with 1.2 μs long pulses for the gate, and 1 μs long pulses for the drain on an AMCAD AM3200 pulsed-IV system. The period between pulses in the pulsed-IV measurements was set to 200 ms to allow for enough time for trap emission in all bias conditions. Note that a portion of the self-bias current under the pulsed class-B operation was observed to leak through to the RF path due to its short duration (0.2 μs). This effect has been observed in other pulsed measurements [19]. To correct for this bias-tee artifact, the drain currents at the peak drain voltage in all pulsed measurements were aligned with that of the CW measurement. The correction from the current measured in the dc path is at most 3 mA.

While the excitation period for these measurements was set to 200 ns (ten periods of 50 MHz), it is important to note that the real-time NVNA measured some transient behavior from the device for the first 120 ns (six periods) of the pulsed-ALP. This is a result of the transistor requiring some time to establish class-B operation. The measured loadlines are therefore the first stabilized loadlines measured after this transient period. While the waveforms measured during the

transient period are not displayed in Fig. 5, the transistor is still experiencing a stable, large drain voltage swing, and therefore this transient period counts toward τ_{RF} (RF excitation time) of 200 ns.

In addition, since the calibration is applied period by period some discontinuities can be observed in the voltage and current waveforms due to their time evolution. These are mostly present during the early stage of the pulse. For example the discontinuities relative to the displayed and adjacent period in Fig. 6(a) was 1.01% of the peak current and 0.31% of the voltage swing. These discontinuities can be reduced by selecting a higher RF frequency.

Each loadline at pulse 1 (excluding condition A) shows a good agreement with its respective pulsed-IV measurement, indicating that the real-time NVNA is accurately measuring the operation of the device at each bias condition. The loadline corresponding to bias condition A for pulse 1 in Fig. 5(a) displays a $I_{D,MAX}$ value that has noticeably decreased from the knee in the pulsed-IV measurement. This is an indication that even pulsing to the PQ bias point contributes to rapid and potent degradation of the device's performance. A loadline from the final pulse (400) of the pulsed-ALP is also plotted. These loadlines show varying levels of degradation from the initial pulse's loadline and pulsed-IV curve and tend to mirror the effects observed as the cumulative excitation time increases in the measurements in Section IV-E. In each class-B loadline, excluding condition C, a noticeable contraction in the drain current swing is observed between pulse 1 and 400, due to the cyclostationary effect (trapping induced by the instantaneous RF voltage).

For comparison, the loadline captured from the CW measurement was used to determine the harmonic terminations of the pulsed-ALP loadline is plotted in Fig. 5(a)–(e) using a thick, gray line. Since it was measured in the CW regime, this loadline is therefore affected by self-heating, dc bias trapping, and cyclostationary trapping. From the conditions tested, the transistor's state in bias condition D is the closest to the CW state, given the device temperature and dc drain bias were set to match the transistor in the CW state. Note that the dc gate bias in both conditions (D and CW) are close enough (0.24 V difference) so that they have similar levels of trapping induced by the gate bias (gate-lag effect). Indeed, we see from the pulsed-IV and pulsed-ALP at pulse 1 in Fig. 5(d), after biasing the device to condition D, that much of the device's degradation from its room-temperature unbiased state (condition A) is caused by trapping from the drain bias and self-heating. The pulsed-ALP loadline captured at pulse 400 closely overlaps with the CW loadline, indicating that the cumulative cyclostationary trapping dynamics observed in the device when pulsed from bias condition D are consistent with the CW operation of the device.

Comparing the pulsed-ALP loadline for condition B in Fig. 5(b) with the CW loadline indicates that just dc biasing the device at $V_{DS,dc}$ while keeping the device off between pulses, slightly underestimates the device's current collapse at both pulse 1 and 400 as condition B does not account for self-heating.

Comparing the pulsed-ALP loadlines for condition C in Fig. 5(c) with the CW loadline also indicates that simply

This article has been accepted for inclusion in a future issue of this journal. Content is final as presented, with the exception of pagination.

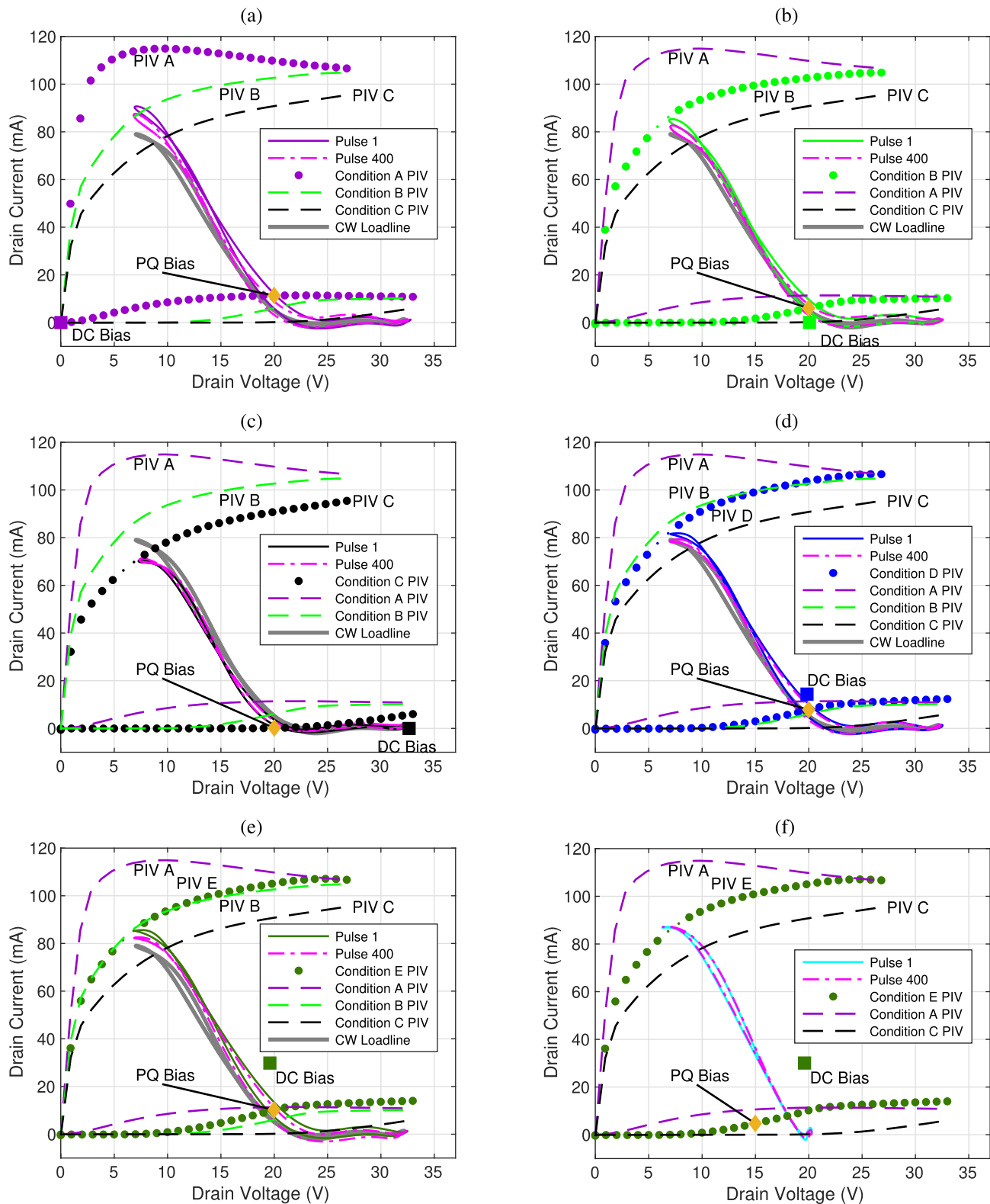LINDQUIST et al.: ISOTHERMAL CHARACTERIZATION OF TRAPS IN GaN HEMTs OPERATING IN CLASS B 9

Fig. 5. IV plots displaying the pulsed loadlines (duty rate of 0.2%) from the beginning (pulse 1) and end (pulse 400) of the pulsed ALP sequence. The pulsed-IV (duty rate of 0.0005%) measured for $v_{GS} = -3.25$ V and $v_{GS} = 0$ V, biased at conditions A–E are plotted using filled circles for comparison in (a)–(e). In (f), the isotrap loadlines measured at pulses 1 and 400 overlaid on pulsed-IV curves for $v_{GS} = -3.25$ V and $v_{GS} = 0$ V biased at condition E are plotted. In addition, the pulsed-IV measured for conditions A–C are plotted using dashed lines for visual reference in each figure. (a) Condition A. (b) Condition B. (c) Condition C. (d) Condition D. (e) Condition E. (f) Isotrap loadline biased at Condition E.

biasing the device at $V_{DS,MAX}$ overestimates the device's current collapse. Indeed, the $I_{D,MAX}$ of the CW loadline largely exceeds the pulsed-IV and pulsed-ALP measurements at condition C.

The pulsed-ALP loadlines for condition E are shown in Fig. 5(e). In condition E, where the device is heated to an even higher temperature with double the dissipated power at dc than the device experiences in CW operation and condition D,
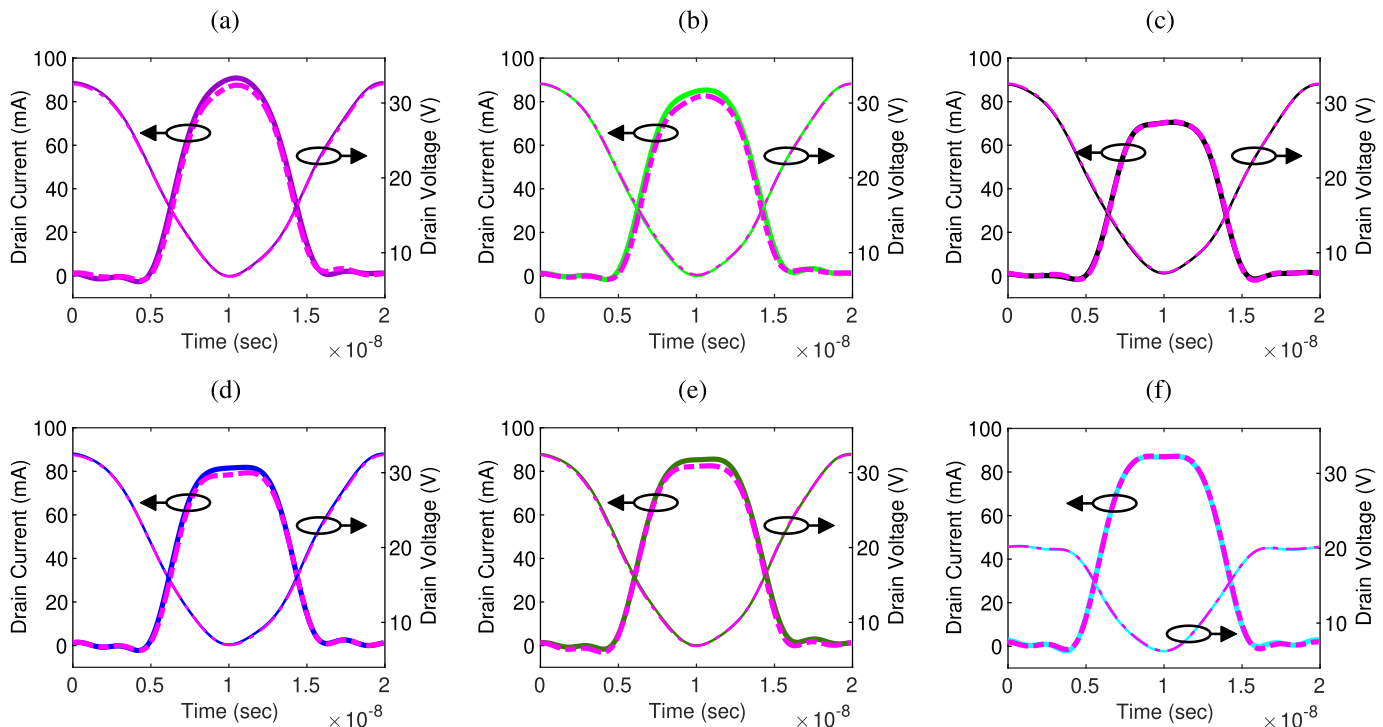
Fig. 6.   Time-domain drain current and voltage waveforms corresponding to the loadlines of pulses 1 and 400 displayed in Fig. 5(a)–(f). The color coding and line styles are the same as shown in the legends in Fig. 5(a)–(f). (a) Condition A. (b) Condition B. (c) Condition C. (d) Condition D. (e) Condition E. (f) Isotrap biased at Condition E.

about the same $I_{D,MAX}$ is observed as in condition B despite the temperature increase. This is assumed to originate from trapping associated with gate-lag that arises from negative gate biasing. This trapping is either due to residual surface trapping after SiN passivation [9], [20] and/or barrier trapping in the AlGaN layer [21]. Upward gate voltage pulses from condition B's more negative gate bias (1 V below the PQ value) to the PQ bias, induce a lower drain current due to gate-lag than pulsing downward from condition E's less negative dc gate bias (0.64 V above the PQ value). The drain current increase from reduced gate-lag compensates for the reduction of the drain current caused by the device's self-heating. Indeed, one can observe in Fig. 5(e) that the pulsed IV's for conditions B and E are very similar at $v_{GS} = 0$ V. This results in a larger drain current swing in the loadlines (pulse 1 and 400) in condition E compared to CW.

Fig. 7 plots the RF power measured at each pulse for each bias condition. Each plot has a moving average with a span of 20 pulses applied to emphasize the trend of the measurement. For conditions A and B, 20 and 15 mW drops in output power can be ascribed to the cyclostationary effect at room temperature, respectively. At elevated temperatures, the drop in output power is lessened to approximately 11 mW for condition D and approximately 6 mW for condition E. Conditions D and E's comparatively smaller power drops are a result of the increased trap emission between pulsed-ALP at higher temperatures of operation (see Section IV-C). The decrease in RF power P_{RF} across the 400 repeated pulses appears to be minor: 6.5% for condition A and 3.8% for condition D. This gives an indication of the relatively small
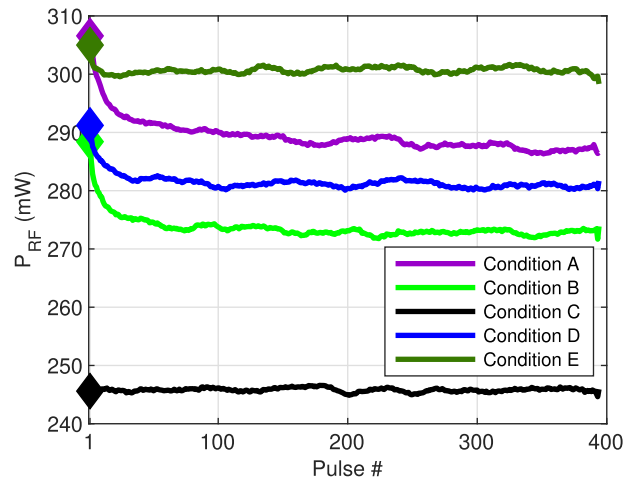

Fig. 7.   Measured transistor RF output power across 400 pulses for each bias condition. A moving average function with a span of 20 pulses was employed to emphasize the trend of the output power. An average standard deviation of 1.8 mW for the raw data from all bias conditions was calculated from the stable period (pulse 150–400).

strength of the cyclostationary effect in this device after the first pulse.

C. Isotrap Pulsed-ALP to Detect Potential Self-Heating

In pulsed measurements, the average increase in device temperature is determined by the pulse duty rate (τ_{pulse}/τ_{dc}). Some self-heating can occur during the application of the pulse even for a few microseconds for devices fabricated on a substrate with low thermal conductivity.
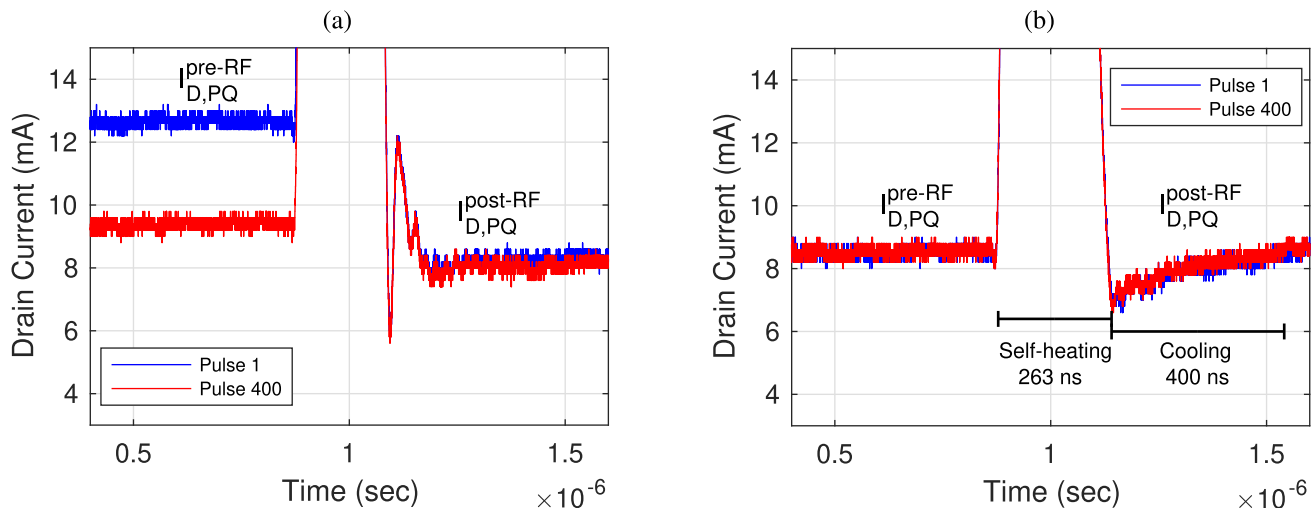
Fig. 8.   Transient drain current plots before and after pulsed-RF application. (a) PQ drain current for condition E loadline. A significant decrease is recorded between $I_{D,PQ}^{pre-RF}$ and $I_{D,PQ}^{post-RF}$, indicating a current collapse caused by trapping via the cyclostationary effect. (b) PQ drain current for the isotrap loadline for condition E biasing. A small dip in $I_{D,PQ}^{post-RF}$ is observed, which is likely caused by slight variations in temperature during the pulse. However, no cumulative cooling effect is observed from pulse 1 to 400.

In this section, we aim to verify that the variation in the post-RF PQ drain current in condition E is not associated with a self-heating effect but is instead due to the cyclostationary effect, largely within the first pulse. For this purpose an isotrap loadline seen in Fig. 5(f) is synthesized to demonstrate pulsed-RF operation of the transistor *without* the cyclostationary effect. The trapping is suppressed by keeping the instantaneous drain voltage $v_{DS}(t)$ smaller or equal to the dc bias voltage $V_{DS,dc}$ at all times when the RF excitation is applied. This is achieved by operating the device with a loadline where *both* the voltage and current waveforms are half-wave rectified, which prevents the device's voltage from swinging above the dc bias point and consequently filling additional traps. To construct this loadline, the impedances presented to all the harmonics are set equal to the fundamental load impedance R_L. The transistor is dc biased at condition E ($V_{GS,dc} = -2.61$ V, $V_{DS,dc} = 20$ V) to set a steady-state trap occupation and temperature. From this state, the transistor is pulsed down to $V_{GS,PQ} = -3.25$ V and $V_{DS,PQ} = 15$ V. The shift down to 15 V reduces the PQ drain current due to the large drain conductance at low gate voltages. Visible in Fig. 8(b) is a slight dip in PQ current immediately after the RF pulse that recovers in approximately 400 ns. The RF response elevates the dissipated power of the transistor for approximately 263 ns. Based on the temporal symmetry of this response, this is likely an indication of slight self-heating that occurs as a result of the pulsed-ALP. Thermometry studies of GaN such as [23] conclude that self-heating in GaN HEMTs can be attributed to a broad spectrum of time constants, with some as fast as 126 ns. This would also indicate that there is some cooling that occurs when the transistor pulses from the dc bias point to the PQ bias point, though as the post-RF current dip shows, the effect of self-heating at these time scales has relatively minor effect on the device's drain current. Indeed, no such effect is observed when swinging above $V_{DS,dc}$ in Fig. 8(a), as it is obscured by the effect of

the device's trapping. Despite the minor temperature variations during the pulse, there is no change in the isotrap loadline's PQ current across the experiment from pulse 1 to 400, indicating that there is no cumulative temperature shift at the chosen duty rate. Note that both the isotrap loadline and the class-B loadline dissipate the same RF power given the isotrap loadline has the same 50% duty cycle. For the isotrap measurement there is no precipitous drop observed in the PQ bias current after the pulsed-ALP ($I_{D,PQ}^{post-RF}$), in marked contrast to the class-B measurement. Clearly, this indicates the isotrap loadline is neither affected by cumulative self-heating nor additional trapping from the cyclostationary effect. From this, we conclude that the significant current drop observed immediately after the application of class-B pulsed-ALP is the result of cyclostationary trapping and not cumulative self-heating. The DUT in this work is a GaN HEMT fabricated on a SiC substrate that has been subsequently thinned to 100 μm and mounted on a metal shim which provides more efficient heat transfer away from the device. Different behavior might be observed for GaN HEMTs on substrates of different materials and thicknesses.

D. Emission Relaxation

With the real-time NVNA presented, it is also possible to measure the PQ drain bias current immediately before ($I_{D,PQ}^{pre-RF}$) and after ($I_{D,PQ}^{post-RF}$) the application of a short burst of the RF signal. When the quiescent and RF pulses are applied, traps will cumulatively capture electrons with each pulse with some emission taking place in between the pulses. In this section and Section IV-E, emission and capture experiments are carried out on a second 2×50 μm GaN HEMT from the same wafer with the biasing conditions and similar RF excitations reported in Section IV-B.

The emission relaxation process can be characterized by adjusting the length of the dc period (τ_{dc}) between RF

This article has been accepted for inclusion in a future issue of this journal. Content is final as presented, with the exception of pagination.

12

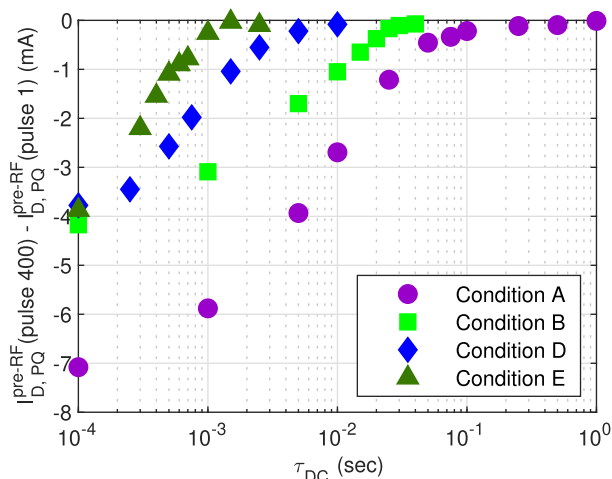IEEE TRANSACTIONS ON MICROWAVE THEORY AND TECHNIQUES

Fig. 9. Emission curves for each bias condition calculated from the difference in pre-RF PQ currents ($I_{D,PQ}^{pre-RF}$) between the final pulse and first pulse for varying τ_{dc} (pulse rates) with constant τ_{RF}.
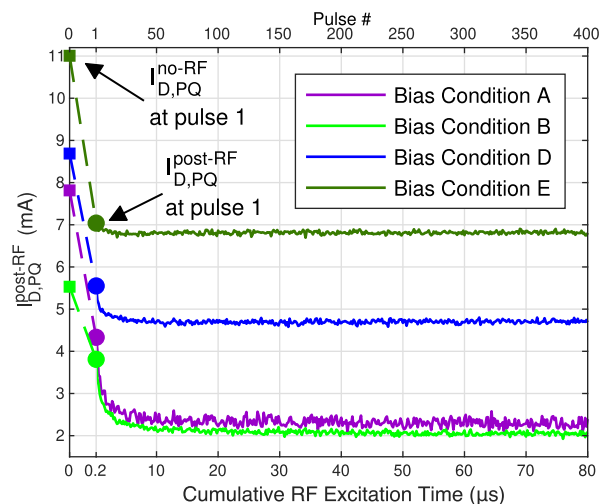

Fig. 10. Current decay curves showing 1) PQ bias current measured from the first pulse when no RF is applied (square) where no cyclostationary trapping has occurred and 2) the variation in post-RF PQ bias current (line) immediately after each class-B pulse as a function of cumulative RF excitation time. The data was taken over 400 consecutive pulses 100 μs apart (τ_{dc}), with an RF excitation time of 200 ns per pulse.

excitations (rest time) while keeping τ_{RF} constant. By measuring the pre-RF PQ current for each pulse at different values of τ_{dc}, we can vary the device recovery through trap emission compensating trap capture performed by the successive applications of the pulsed-ALP. As the time between pulses increases, more traps will emit their electrons, reducing and eventually negating the decrease in the pre-RF PQ current in subsequent pulses. Relaxation of the quiescent current to the reference quiescent current: $I_{D,PQ}^{pre-RF}$ (pulse 1) $\simeq$ $I_{D,PQ}^{pre-RF}$ (final pulse), is observed to take place at several different orders of magnitude of τ_{dc} based on the bias and temperature of the device. At this emission recovery time, the emission process during the rest dc period fully negates the capture process during the RF period (and bias period for condition A) at each pulse. This emission recovery time is really a measure of the collective emission time in the device since the device response is most likely affected by an ensemble of spatially distributed traps.

The same measurements were performed for the biasing conditions A, B, D, and E. They are reported in Fig. 9 for pulse 400 at which steady state is reached.

When biased at $V_{DS,MAX}$ for condition C, the transistor does not experience any measurable change in PQ drain current between pulses because the instantaneous peak RF voltage $v_{DS,pk}$ is approximately equal to the $V_{DS,dc}$ of condition C and there is not a significant change in trap occupation from the pulsed-ALP. As a result, condition C is excluded from Fig. 9.

For bias conditions D and E, the transistor's gate is biased above the transistor's threshold voltage (V_{th}) so that a current flows through the transistor's channel, and the resultant dc power is dissipated as heat between pulses. Bias condition D is meant to mimic the self-heating experienced by the transistor during CW class-B operation. The self-heating of the transistor while the pulsed-ALP is inactive is observed to have a significant effect on the emission of electrons by the device's traps. The pre-RF PQ drain current appears to fully recover to its initial state after a dc period of ten milliseconds. This effect is accelerated (smaller emission recovery time) as

the temperature increases for bias condition E, where the dc power dissipated as heat is twice what it is in bias condition D and the measured total emission time drops to as low as 1 ms. This is to be expected and is characterized in [14], as thermal emission of carriers from the traps.

E. Capture Process

Trap capture via the cyclostationary effect when the RF pulse is applied (yielding $v_{DS}(t) > V_{DD}$ for half the period) occurs very quickly, with the majority of the PQ bias current decrease measured after the first pulsed-ALP application. Fig. 10 compares the post-RF PQ current measured immediately after the application of pulsed class-B ALP (dot and line) and the PQ current measured at the same point in the pulse in a separate measurement where no pulsed-ALP is performed (square) for the different bias conditions. The current measurement with no RF is the value of the PQ drain current with no cyclostationary trapping. In Fig. 10, the time scale for the first pulse (0–200 ns) is magnified to highlight the very fast initial decay (dashed line). The initial current measured at each condition differs in Fig. 10; the decrease between conditions A and B arises from the drain bias (drain lag), whereas the increase in initial PQ current from conditions B to D to E, is a result of reduced gate lag from the less negative gate bias.

For bias condition A, cyclostationary trapping is observed to drop the PQ drain current by 3.5 mA in the first pulse, then a gradual additional decrease of 2 mA occurs in the following pulses until the device settles at a post-RF PQ drain current of 2.3 mA. This indicates that the first pulse of both the drain quiescent bias and RF excitation fills a great number of the transistor's traps starting from the untrapped state. Bias condition B shows a smaller initial decrease of 1.7 mA of PQ drain current in the first pulse from the initial value of 5.5 mA and reaches a steady state current of 2 mA after 20 μs
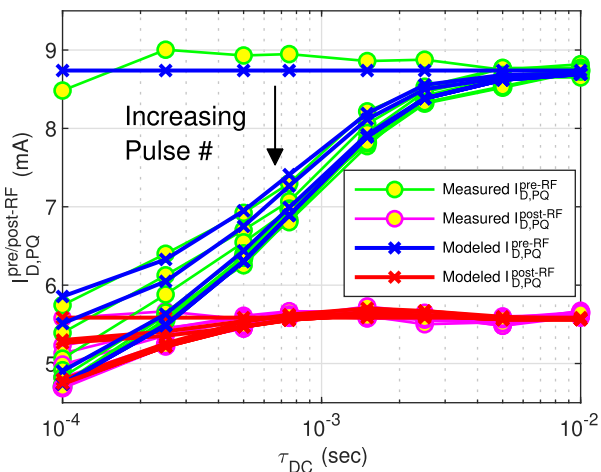
Fig. 11. Plot of the measured and modeled PQ drain current at various values of τ_{dc}. $I_{D,PQ}^{pre\text{-}RF}$ and $I_{D,PQ}^{post\text{-}RF}$ at pulses 1, 2, 3, 6, 15, 30, 75, and 400 are plotted for bias condition D.

(100 pulses) of cumulative RF excitation because many of the transistor's traps were already filled by the dc bias. A similar dynamic for the decrease in current was reported in [8] where both short and long timescales were observed with the shorter timescale smaller than 1 μs.

For condition D, where the device's bias is set to dissipate power equal to what the transistor experiences during CW, Fig. 10 shows an initial post-RF PQ drain current decrease of 3.1 mA from pulse 1's no-RF PQ current of 8.7 mA which happens after the first burst of pulsed-ALP. The post-RF PQ drain subsequently drops another 0.9 mA in the next 50 pulses to reach 4.7 mA. At the higher device temperature experienced in bias condition E, an initial decrease of 4 mA is recorded, and the current very slightly decreases by 0.2 mA in approximately ten pulses to reach a steady state of 6.8 mA. Controlling for the same drain bias in conditions B, D, and E, it is observed that increasing the temperature of the device prevents traps from significantly reducing the drain current in subsequent pulses. This is an indication that the traps responsible for the cumulative current decrease in pulses 2–400 will emit on a shorter time scale. This is consistent with the data in Table VI where all the relaxation times $\tau_{i,off}$ (extracted in Section IV-F) decrease by at least a factor of 5 when increasing the operating temperature from conditions B to E.

In summary, the dynamic observed and modeled for conditions B, D, and E, shows that the temperature of the transistor decreases the ability of traps in GaN HEMTs to retain electrons for significant amounts of time. From this data, we can also conclude that the initial trapping effect from the cyclostationary effect captures traps extremely quickly, as every bias condition biased below $V_{DS,MAX}$ exhibits a noticeable decrease in the transistor's bias current after even the first application of pulsed-ALP.

F. Trap Modeling

Fig. 11 shows the pre-RF and post-RF PQ drain currents of the transistor-biased in condition D measured at different pulses for various values of τ_{dc} between pulses. Convergence

has been established by pulse 400 for all values of τ_{dc}. Trapping studies such as [11] demonstrate that the emission and capture processes for GaN HEMTs are distributed, and require a model with multiple relaxation time constants. An SRH behavioral trap model similar to that in [11] is presented in the Appendix B and used to approximate the trapping behavior of the device under pulsed operation. The measurement at condition D in particular was chosen to be displayed to analyze the behavior of trapping via the cyclostationary effect when the device's drain bias and temperature match those of the device in CW class-B operation. The initial trap occupation before the RF is applied is thus due to the set drain bias, with further drain current degradation resulting from self-heating. A distributed trap model is employed, with three different emission and capture constants extracted. These values are reported in Table VI. Of note is the submicrosecond capture time constant, which reflects the approximately 3.5 mA decrease from $I_{D,PQ}^{pre\text{-}RF}$ to $I_{D,PQ}^{post\text{-}RF}$ after the first 200 ns RF pulse. Minimal emission is observed at the fastest repetition rate where $\tau_{dc} = 100$ μs as indicated by the very small (0.05 mA) difference pre-RF and post-RF PQ drain current measurements at pulse 400 and the pulses approaching it. This can also be seen in Figs. 11 and 12 in Appendix B. This is to be expected because τ_{dc} is then much smaller than the shortest emission time in Table VI such that the traps do not have time to emit. On the other hand when the rest time τ_{dc} is larger than the largest value of $\tau_{i,off}$ for condition D in Table VI (6.3 ms) all the traps have enough time to fully emit and return to their occupation state in the dc operating point condition. This is observed in Fig. 11 where the device drain current returns to its initial pre-RF PQ drain current when the device rests for a time τ_{dc} of 10 ms between pulses. For intermediate values of the rest time τ_{dc}, the pre-RF and post-RF PQ drain currents rapidly converge to intermediate values between the extreme values of pre-RF and post-RF PQ drain currents as emission partially hinders the capture process. Note that for values of τ_{dc} of 750 μs and above, the post-RF PQ current $I_{D,PQ}^{post\text{-}RF} \approx 5.5$ mA is nearly constant after one RF pulse indicating the efficacy of the emission process when τ_{dc} is large enough. Note in Fig. 11, the larger dispersion in pre-RF PQ current (green) versus post-RF PQ current (magenta) during the cumulative capture process. This effect is accounted for in the trapping model of Appendix B by the 2nd-order nonlinear dependence of the device IV on the trap occupations N_i when the gate voltage is close to the threshold voltage. The relaxation measurements reported in Fig. 11 bear some similarity to the two-tone measurements
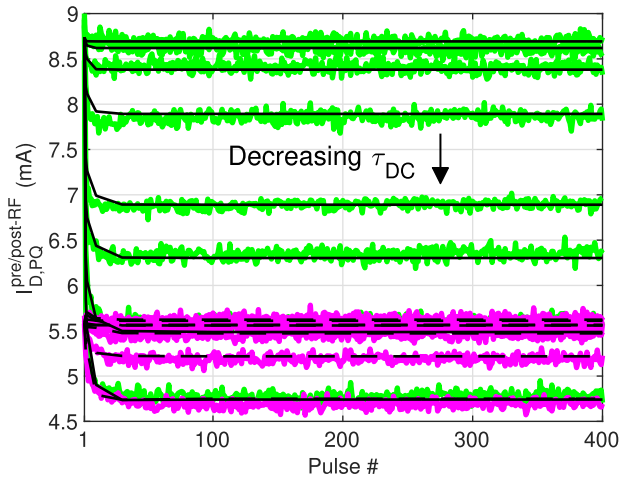
Fig. 12.   Curves showing the decrease in the pre-RF (green) and post-RF (magenta) PQ drain current as the pulses proceed. The data plotted is the same as is seen in Fig. 11. The black lines overlaid correspond to the modeled pre-RF (solid) and post-RF (dashed) drain current generated by (9). The curves for the various τ_{dc} are shown in descending order with smaller τ_{dc} values corresponding to the deeper curves.

reported in [13, Fig. 6] with the τ_{dc} corresponding to the tone spacing. Indeed for small tone spacing the device has time to recover at the envelope minimum. Note, however, that for small tone spacing (10 Hz) the measurement in [13] is exciting both self-heating and trapping and is thus not isothermal. In contrast, only the trapping process is activated in the pulsed relaxation measurement reported in Fig. 11, as is demonstrated in Section IV-B. However, the SRH reported in [13] can be adapted to model the device response under pulsed operation.

V. Conclusion

In this article, we have reported an improved real-time NVNA testbed which made it possible to study the isothermal transient response of a GaN HEMT operating in the power-efficient class-B mode. For this purpose, a pulsed multiharmonic ALP relying on a two-channel AWG for the gate and drain was developed for use with the real-time NVNA. Furthermore, the harmonic phase calibration of the real-time NVNA was also implemented with an AWG. This provides a more cost-effective option than the use of an external NVNA for the harmonic phase calibration as was done in our previous work [1]. A rigorous traceability study was also performed to account for nonlinearities present in the testbed's oscilloscope and calibration AWG. This included characterizing *phase* dispersions introduced by the input stage and scaling circuitry of the oscilloscope, the AWG, and its HPR access line, as well as *magnitude* discrepancies introduced from the oscilloscope's scaling circuitry.

To demonstrate the application of this improved real-time NVNA, a GaN HEMT operating in class B at five different isothermal biasing conditions was characterized to study the impact of trapping via drain biasing and temperature relative to the cyclostationary effect.

The real-time NVNA facilitated the capture of the RF dynamic loadlines from pulse to pulse with 400 pulses acquired using segmented memory. The capture and emission

times were acquired from the PQ currents preceding and following the RF pulses. These measurements demonstrated that a majority of the capture process is taking place in the first RF pulse (<200 ns) with the residual capture process distributed over various durations depending on the biasing condition. For bias condition A, where the transistor had no drain bias applied, a precipitous decrease of $I_{D,MAX}$ compared to the pulsed-IV measurement is measured. This is an indication that for RF operation of GaN HEMTs, trapping from the drain bias is so fast that the RF performance predicted by the pulsed-IV curves is impossible to achieve in practice. The investigation of the temperature dependence for the case of room temperature, CW class-B operating temperature, and a further increased temperature (conditions B, D, and E, respectively) demonstrated that the emission time is greatly decreased at higher temperatures. The trap dynamics of the transistor biased at conditions B, D, and E were analyzed with a behavioral trap model. The loadlines measured by the real-time NVNA at this biasing condition showed that the cumulative trapping from the repeated pulsed-ALP introduced the same current collapse as is seen in the CW loadline. These real-time, pulsed NVNA measurements are able to distinguish between the relative effects of cyclostationary trapping and self-heating in GaN HEMTs for pulses of short duration, which due to their common effect (current collapse) and their interdependent origin: drain bias and power dissipation, respectively, are difficult to separate in most standard measurements.

This study of trapping in GaN HEMTs demonstrates that the proposed real-time NVNA combined with pulsed multiharmonic ALP provides a useful tool to isothermally study the dynamics of trapping in RF devices operating along arbitrary loadlines with detail that cannot be readily resolved using equivalent-time NVNAs.

Appendix A

An error in one of the equations previously published by Lindquist et al. [1] is corrected in this section. Equation (3) should read

$$\frac{A_1(n\omega)}{A_1(\omega)} = \frac{a_{1,M}(n\omega)}{a_{1,M}(\omega)} \frac{a_1(\omega) + B_1'(\omega)b_1(\omega)}{a_1(n\omega) + B_1'(n\omega)b_1(n\omega)}.$$

Appendix B

The SRH model equation for a single acceptor-like trap is given by [11, Equ. (2)] with the assumption that the trap is located in a nondegenerate semiconductor with the electron population following the Maxwell–Boltzmann statistics. The solution to this equation for a trap i is then

$$n_{T,i}(t) = \left(n_{T,i}(0) - N_{T,i}^\infty\right)e^{\frac{-t}{\tau_i}} + N_{T,i}^\infty$$

where τ_i the trap relaxation time-constant and $N_{T,i}^\infty$ the steady-state trap occupation are given by

$$\frac{1}{\tau_i(F_i)} = c_{n,i}N_c e^{\frac{E_{T,i}-E_c}{kT}}\left(1 + e^{\frac{F_i-E_{T,i}}{kT}}\right)$$

$$N_{T,i}^\infty = n_{T,i}(\infty) = \frac{N_{T,i}}{1 + e^{-\frac{F_i-E_{T,i}}{kT}}}$$

This article has been accepted for inclusion in a future issue of this journal. Content is final as presented, with the exception of pagination.

LINDQUIST et al.: ISOTHERMAL CHARACTERIZATION OF TRAPS IN GaN HEMTs OPERATING IN CLASS B

15

where $c_{n,i}$ is the electron capture coefficient, $N_{T,i}$ is the trap density, N_c is the effective density of states, F_i is the quasi-Fermi level, k is the Boltzmann's constant, and T is the local temperature. When no signal RF is applied (OFF) but just the targeted dc bias voltage for a duration τ_{dc}, the trap relaxation time τ_i will be noted τ_i^{off}. For infinite τ_{dc} time, the trap concentration $n_{T,i}(t)$ will relax to a constant value noted $N_{T,i}^{\infty} = N_{T,i}^{off}$. When the large-signal RF voltage is applied (ON) to the device, the trap i is submitted to a fast time-varying Fermi level $F_i(t)$. According to the cyclostationary theory [17], the effective trap relaxation rate noted τ_i^{on} is given by the trap generation rate $1/\tau_i(t)$ averaged over the RF period

$$\frac{1}{\tau_{i,\text{on}}} = \frac{1}{T}\int_t^{t+T}\frac{1}{\tau_i(F_i(t))}dt.$$

For infinite τ_{RF} time, the trap concentration $n_{T,i}(t)$ will relax to a constant value noted $N_{T,i}^{on}$.

The evolution of the prepulse and postpulse trap concentrations from pulse to pulse is then given at pulse p by the equations

$$n_{T,i}^{post}(p) = \left(n_{T,i}^{pre}(p) - N_{T,i}^{on}\right)e^{-\frac{\tau_{RF}}{\tau_{i,\text{on}}}} + N_{T,i}^{on}$$
$$n_{T,i}^{pre}(p+1) = \left(n_{T,i}^{post}(p) - N_{T,i}^{off}\right)e^{-\frac{\tau_{dc}}{\tau_{i,\text{off}}}} + N_{T,i}^{off}. \quad (8)$$

It results from this iterative process that at any pulse p, the prepulse and postpulse trap occupation concentrations $n_{T,i}^{post}(p)$ and $n_{T,i}^{pre}(p)$ are both proportional to $n_{T,i}(0)$, $N_{T,i}^{off}$, and $N_{T,i}^{on}$. We will only monitor the unoccupied traps so that we have $n_{T,i}^{pre}(0) = N_{T,i}^{\infty} = 0$ when the experiment is started.

After a large enough number of pulses, the prepulse and postpulse trap occupation concentrations reach the steady state values

$$n_{T,i}^{post}(\infty) = \frac{e^{-\frac{\tau_{RF}}{\tau_{i,\text{on}}}}\left(1 - e^{-\frac{\tau_{dc}}{\tau_{i,\text{off}}}}\right)N_{T,i}^{off} + \left(1 - e^{-\frac{\tau_{RF}}{\tau_{i,\text{on}}}}\right)N_{T,i}^{on}}{1 - e^{-\frac{\tau_{RF}}{\tau_{i,\text{on}}} - \frac{\tau_{dc}}{\tau_{i,\text{off}}}}}$$

$$n_{T,i}^{pre}(\infty) = \frac{\left(1 - e^{-\frac{\tau_{dc}}{\tau_{i,\text{off}}}}\right)N_{T,i}^{off} + e^{-\frac{\tau_{dc}}{\tau_{i,\text{off}}}}\left(1 - e^{-\frac{\tau_{RF}}{\tau_{i,\text{on}}}}\right)N_{T,i}^{on}}{1 - e^{-\frac{\tau_{RF}}{\tau_{i,\text{on}}} - \frac{\tau_{dc}}{\tau_{i,\text{off}}}}}.$$

To first order, the prepulse and postpulse quiescent currents could be assumed to be linearly perturbed by the individual trap occupation concentrations. However, since the pulsed quiescent bias gate voltage is close to the threshold voltage, a second-order perturbation is found to be necessary to account for the different dispersion in pre-RF and post-RF PQ drain currents. The evolution of the prequiescent and postquiescent currents is then given by

$$I_{D,PQ}^{post}(p) = I_{D,PQ}^{post}(0) + \sum_{i=1}^{n_i}C_i^{1st}n_{T,i}^{post}(p)$$
$$+ \sum_{i=1}^{n_i}\sum_{j=i}^{n_i}C_{i,j}^{2nd}n_{T,i}^{post}(p)n_{T,j}^{post}(p)$$
$$I_{D,PQ}^{pre}(p) = I_{D,PQ}^{pre}(0) + \sum_{i=1}^{n_i}C_i^{1st}n_{T,i}^{pre}(p)$$
$$+ \sum_{i=1}^{n_i}\sum_{j=i}^{n_i}C_{i,j}^{2nd}n_{T,i}^{pre}(p)n_{T,j}^{pre}(p). \quad (9)$$

Given the prepulse and postpulse quiescent drain currents measured, nonlinear least squares and linear least squares are jointly performed to extract the time constants $\tau_{i,\text{off}}$ and $\tau_{i,\text{on}}$ and the weighted trap occupation concentrations $C_i^{1st}N_{T,i}^{on}$ and $C_{i,j}^{2nd}N_{T,i}^{on}N_{T,j}^{on}$, respectively. The time constants extracted are reported in Table VI and the modeling results obtained are shown in Figs. 11 and 12. These results are reviewed in Section IV-F.

REFERENCES

[1] M. Lindquist, P. Roblin, and N. C. Miller, "New real-time pulsed-RF NVNA testbed for isothermal characterization of traps in GaN HEMTs," in *IEEE MTT-S Int. Microw. Symp. Dig.*, San Diego, CA, USA, Jun. 2023, pp. 1026–1029.

[2] J. Verspecht, P. Debie, A. Barel, and L. Martens, "Accurate on wafer measurement of phase and amplitude of the spectral components of incident and scattered voltage waves at the signal ports of a nonlinear microwave device," in *IEEE MTT-S Int. Microw. Symp. Dig.*, Orlando, FL, USA, May 1995, pp. 1029–1032, doi: 10.1109/MWSYM.1995.406147.

[3] P. Blockley, D. Gunyan, and J. B. Scott, "Mixer-based, vector-corrected, vector signal/network analyzer offering 300 kHz-20 GHz bandwidth and traceable phase response," in *IEEE MTT-S Int. Microw. Symp. Dig.*, Long Beach, CA, USA, Jun. 2005, pp. 1497–1500, doi: 10.1109/MWSYM.2005.1516977.

[4] M. A. Chaudhary, J. Lees, J. Benedikt, and P. Tasker, "A sampling oscilloscope based system with active RF/IF load-pull for multi-tone non-linear device characterization," *Int. J. Microw. Opt. Technol.*, vol. 8, no. 3, pp. 112–119, May 2013.

[5] A. Raffo, F. Scappaviva, and G. Vannini, "A new approach to microwave power amplifier design based on the experimental characterization of the intrinsic electron-device load line," *IEEE Trans. Microw. Theory Techn.*, vol. 57, no. 7, pp. 1743–1752, Jul. 2009, doi: 10.1109/TMTT.2009.2022816.

[6] M. Molina-Ceseña, J. A. Reynoso-Hernández, M. A. Pulido-Gaytán, J. R. Loo-Yau, and M. C. Maya-Sánchez, "Experimental investigation of resistive–reactive class-J mode using time-domain low-frequency active harmonic load–pull measurements," *IEEE Microw. Wireless Compon. Lett.*, vol. 32, no. 1, pp. 96–99, Jan. 2022, doi: 10.1109/LMWC.2021.3113289.

[7] A. E. Parker and J. G. Rathmell, "Measurement and characterization of HEMT dynamics," in *Proc. Asia–Pacific Microw. Conf.*, Sydney, NSW, Australia, Nov. 2000, pp. 846–849, doi: 10.1109/APMC.2000.925962.

[8] M. J. Uren, J. Moreke, and M. Kuball, "Buffer design to minimize current collapse in GaN/AlGaN HFETs," *IEEE Trans. Electron Devices*, vol. 59, no. 12, pp. 3327–3333, Dec. 2012, doi: 10.1109/TED.2012.2216535.

[9] S. C. Binari, P. B. Klein, and T. E. Kazior, "Trapping effects in GaN and SiC microwave FETs," *Proc. IEEE*, vol. 90, no. 6, pp. 1048–1058, Jun. 2002, doi: 10.1109/JPROC.2002.1021569.

[10] M. Meneghini et al., "Buffer traps in Fe-doped AlGaN/GaN HEMTs: Investigation of the physical properties based on pulsed and transient measurements," *IEEE Trans. Electron Devices*, vol. 61, no. 12, pp. 4070–4077, Dec. 2014, doi: 10.1109/TED.2014.2364855.

[11] J. L. Gomes, L. C. Nunes, C. F. Goncalves, and J. C. Pedro, "An accurate characterization of capture time constants in GaN HEMTs," *IEEE Trans. Microw. Theory Techn.*, vol. 67, no. 7, pp. 2465–2474, Jul. 2019.

[12] W. Shockley and W. T. Read Jr., "Statistics of the recombinations of holes and electrons," *Phys. Rev.*, vol. 87, pp. 835–842, Sep. 1952, doi: 10.1103/PhysRev.87.835.

[13] P. M. Tomé, F. M. Barradas, L. C. Nunes, J. L. Gomes, T. R. Cunha, and J. C. Pedro, "Characterization, modeling, and compensation of the dynamic self-biasing behavior of GaN HEMT-based power amplifiers," *IEEE Trans. Microw. Theory Techn.*, vol. 69, no. 1, pp. 529–540, Jan. 2021.

[14] M. Cioni et al., "Electric field and self-heating effects on the emission time of iron traps in GaN HEMTs," *IEEE Trans. Electron Devices*, vol. 68, no. 7, pp. 3325–3332, Jul. 2021, doi: 10.1109/TED.2021.3081613.

[15] Y. Ko, P. Roblin, C. Kai Yang, H. Jang, and B. Poling, "New thermometry and trap relaxation characterization techniques for AlGaN/GaN HEMTs using pulsed-RF excitations," in *IEEE MTT-S Int. Microw. Symp. Dig.*, Jun. 2012, pp. 1–3.

[16] G. P. Gibiino, A. Santarelli, and P. A. Traverso, "Pulsed techniques for the characterization of low-frequency dispersive effects in RF power FETs using a flexible measurement set-up," *Measurement*, vol. 176, May 2021, Art. no. 109240, doi: 10.1016/j.measurement.2021.109240.

[17] A. S. Roy and C. C. Enz, "Analytical modeling of large-signal cyclostationary low-frequency noise with arbitrary periodic input," *IEEE Trans. Electron Devices*, vol. 54, no. 9, pp. 2537–2545, Sep. 2007.

[18] J. Verspecht, "Large-signal network analysis," *IEEE Microw. Mag.*, vol. 6, no. 4, pp. 82–92, Dec. 2005, doi: 10.1109/MMW.2005.1580340.

[19] S. J. Doo et al., "Effective suppression of IV knee walk-out in AlGaN/GaN HEMTs for pulsed-IV pulsed-RF with a large signal network analyzer," *IEEE Microw. Wireless Compon. Lett.*, vol. 16, no. 12, pp. 681–683, Dec. 2006.

[20] R. C. Fitch et al., "Comparison of passivation layers for AlGaN/GaN high electron mobility transistors," *J. Vac. Sci. Technol. B, Nanotechnol. Microelectron., Mater., Process., Meas., Phenomena*, vol. 29, no. 6, Nov. 2011, Art. no. 061204, doi: 10.1116/1.3656390.

[21] N. K. Subramani, J. Couvidat, A. A. Hajjar, J.-C. Nallatamby, R. Sommet, and R. Quéré, "Identification of GaN buffer traps in microwave power AlGaN/GaN HEMTs through low frequency S-parameters measurements and TCAD-based physical device simulations," *IEEE J. Electron Devices Soc.*, vol. 5, no. 3, pp. 175–181, May 2017, doi: 10.1109/JEDS.2017.2672685.

[22] S. Gustafsson, M. Thorsell, J. Stenarson, and C. Fager, "An oscilloscope correction method for vector-corrected RF measurements," *IEEE Trans. Instrum. Meas.*, vol. 64, no. 9, pp. 2541–2547, Sep. 2015, doi: 10.1109/TIM.2015.2407451.

[23] K. R. Bagnall, O. I. Saadat, S. Joglekar, T. Palacios, and E. N. Wang, "Experimental characterization of the thermal time constants of GaN HEMTs via micro-Raman thermometry," *IEEE Trans. Electron Devices*, vol. 64, no. 5, pp. 2121–2128, May 2017, doi: 10.1109/TED.2017.2679978.

Patrick Roblin (Senior Member, IEEE) received the Maîtrise de Physics degree from Louis Pasteur University, Strasbourg, France, in 1980, and the D.Sc. degree in electrical engineering from Washington University in St. Louis, St. Louis, MO, USA, in 1984.

In 1984, he joined the Department of Electrical Engineering, The Ohio State University (OSU), Columbus, OH, USA, where he is currently a Professor. He is the Founder of the Nonlinear RF Research Laboratory, OSU. He has also developed two educational RF/microwave laboratories and associated curriculum for training both undergraduate and graduate students at OSU. He has authored or coauthored three textbooks (two published by Cambridge University Press and one by Springer). His present research interests include the measurement, modeling, design, and linearization of nonlinear RF devices and circuits such as power amplifiers and MIMO systems.

Dr. Roblin served as a Distinguished Microwave Lecturer for IEEE-MTT in 2016, 2017, and 2018.

Dominic Mikrut (Graduate Student Member, IEEE) received the B.Sc. degree in electrical and computer engineering from The Ohio State University, Columbus, OH, USA, in 2018, where he is currently pursuing the Ph.D. degree in electrical and computer engineering.

His current research interests are focused on high-efficiency wideband power amplifiers and nonlinear behavioral modeling.

Matthew J. Nichols (Graduate Student Member, IEEE) received the B.S. degree in electrical and computer engineering from The Ohio State University, Columbus, OH, USA in 2023, where he is currently pursuing the M.S. degree in electrical and computer engineering.

He holds an amateur radio general license. His primary research interests include the measurement and modeling of RF power amplifiers.

Nicholas C. Miller (Senior Member, IEEE) received the B.S., M.S., and Ph.D. degrees in electrical and computer engineering from Michigan State University, East Lansing, MI, USA, in 2013, 2015, and 2017, respectively.

He was an Electronics Engineer at the Air Force Research Laboratory from 2017 to 2023. In 2023, he joined the Faculty of the Electrical and Computer Engineering Department, Michigan State University, as an Assistant Professor. His current research interests include linear and nonlinear mm-wave characterization of on-wafer transistors and integrated circuits, physics-based compact modeling of compound semiconductor transistors, and technology computer-aided design modeling of wide and ultrawide bandgap semiconductor transistors.

Dr. Miller is currently a Young Professional Member of the IEEE MTT TC-3 Microwave Measurements Committee. He was a recipient of the IEEE AP-S Predoctoral Research Award in 2013, the U.S. DoD Science, Mathematics, and Research for Transformation (SMART) Scholarship in 2014, the IEEE Dayton Section Harrell V. Nobel Award in 2019 for physics-based device modeling, the Best Conference Paper Award at the 21st IEEE Wireless and Microwave Technology Conference (WAMICON) in 2021, the Best Presentation Award at the IEEE MTT-S Young Professional Workshop on Optimization and Modeling of Active Devices in 2022, and the AFRL Early Career Award in 2023.

Miles Lindquist (Graduate Student Member, IEEE) received the B.S. degree in physics from Ohio University, Athens, OH, USA, in 2017. He is currently pursuing the Ph.D. degree at The Ohio State University, Columbus, OH, USA.

He worked as a Semiconductor Process Engineer at the Air Force Research Laboratory from 2017 to 2019. He has been a part of Dr. Patrick Roblin's Nonlinear RF Laboratory since 2019 and is primarily focused on the nonlinear modeling and measurement of GaN HEMT devices. His research interests include nonlinear embedding models and trap characterization and modeling.